PCCP

PAPER

Check for updates

Correlation of magnetic resonance (EPR, ssNMR) parameters and crystal-microstrain in marbles as a tool to probe their provenance†

Loukas Belles, [ID] ‡[a] Christos Dimitriou, [ID] ‡[a] Constantinos Moularas,[a] Maria Solakidou, [ID] [a] Marinos Theorodakopoulos, [ID] [b] Maria Louloudi[b] and Yiannis Deligiannakis [ID] *[a]

Marbles constitute a significant family of materials, for antiquities, as well as modern constructions. Herein, we have studied Greek marbles, using electron paramagnetic resonance (EPR) and solid-state nuclear magnetic resonance (ssNMR) spectroscopies, focusing on their structural microenvironment. Spin-Hamiltonian parameters derived from EPR spectra of naturally occurring $^{55}Mn^{2+}$ ($S = 5/2$, $I = 5/2$) atoms in marbles, were studied as structural-probes. EPR data at 300 K provide a library of $^{55}Mn^{2+}$ zero-field-splitting parameters (E, D). The effect of temperature (300 up to 700 K) on $^{55}Mn^{2+}$-ZFS (E, D) and the strain of the **D**-tensor (D_{strain}) was studied by high-temperature EPR spectroscopy. The EPR data, combined with ^{13}C-ssNMR, provide detailed physicochemical information of the calcite and dolomite crystal phases in the marbles. In parallel, we have analyzed the lattice-microstrain (ε_0) of the marbles' crystallites using high-resolution XRD data. Analysis of the correlation between the D-values of Mn^{2+} centers and (ε_0)-XRD, reveals trends that reflect the provenance of the marbles. In this context, we discuss the correlation between the D-values of Mn^{2+} centers and (ε_0)-microstrain as a novel tool to elucidate the provenance of marbles.

1. Introduction

The use of Greek marble in ancient architecture and sculpture has fascinated researchers and historians for centuries.[1] The physicochemical properties of Greek marbles, including their mineral composition, texture, and color, have rendered them a subject of intense study in the field of materials science.[2,3] Identification of the origin of marbles used in monuments is very important.[3] Moreover, the effects of environmental factors, such as temperature and mechanical stress, if properly measured and analyzed, are expected to provide insights into their historical evolution.[1] In fact, it is well recognized that the precise attribution of geographical origin and environmental fingerprints to ancient marbles can provide useful information about cultural linkages.[3–5] A closely related task is to establish scientific tools that allow the interlinking of parts or fragments from various monuments, that have been shattered or

separated.[6] In this context, so far, the characterization of marbles and the determination of their provenance, constitute important archaeological challenges that require use of specific petrographical and physicochemical techniques.[7] Marble is defined as a carbonate rock that has undergone regional or contact metamorphism, according to petrography,[4] in which calcite [$CaCO_3$] or dolomite [$CaMg(CO_3)_2$] composes its crystal lattice.[8] Apart from calcite and dolomite, which are the structural minerals, marble can also contain trace amounts of accessory minerals such as quartz, aluminosilicate minerals (muscovite, chlorite, phlogopite, *etc.*), and in some cases, Fe-oxides and graphite, giving veins of orange or dark color, respectively.[9] Calcite and dolomite are responsible for the typical white color of marble, while impurities and other minerals often contribute to different colors, which vary from white to blue, gray, or even black.[10,11] The whiter the marble stones, the lower the accessory mineral content, and this renders their distinction more difficult. Thus, white marbles are among the most difficult to differentiate with regard to their origin, *i.e.*, due to their broad use in antiquity and lack of distinguishing macroscopic characteristics.[3,5,6]

Calcite is calcium carbonate with a trigonal crystal structure. Insertion of divalent cations, such as Mg^{2+}, Mn^{2+}, Fe^{2+} and Fe^{3+}, creates defects in the calcite microstructure.[12] Thus, techniques

[a] *Laboratory of Physical Chemistry of Materials & Environment, Department of Physics, University of Ioannina, 45110, Ioannina, Greece. E-mail: ideligia@uoi.gr*

[b] *Laboratory of Biomimetic Catalysis & Hybrid Materials, Department of Chemistry, University of Ioannina, 45110 Ioannina, Greece*

31040 | *Phys. Chem. Chem. Phys.*, 2023, **25**, 31040–31049

This journal is © the Owner Societies 2023

such as instrumental neutron activation analysis (INAA),[13] trace element analysis,[14] analysis of stable-isotope ratios using mass spectroscopy,[15] cathodoluminescence,[16] and X-ray diffraction (XRD),[17] have been utilized as high-resolution tools to analyze the composition, structure, and ultimately the origin and geochemical itinerary of white marbles. Magnetic resonance spectroscopies, *i.e.* electron paramagnetic resonance (EPR)[6,8,18] and solid-state NMR (ssNMR) spectroscopies[19] can offer high-precision, high resolution information on the local environment of the marble structures. For example, the ^{13}C-ssNMR spectrum for calcite identified crystal flaws as well as the presence of trace elements, establishing the origin of marble.[19] In a more recent study, in addition to ^{13}C, two extra nuclei, *i.e.*, [25]Mg-ssNMR and [43]Ca-ssNMR, were shown to provide specific information about variations among dolomitic marbles that can assist in their discrimination.[20] It should be underlined, however, that a combination and correlation of information is necessary, not a single technique, to address the complex issue of marble provenance and geochemical itinerary.[21–24]

Herein, we propose a methodological approach based on the concurrent use of magnetic resonance (EPR and ssNMR spectroscopy) together with high-resolution XRD to establish a methodology that will contribute to the analysis of the microstructure of white marbles and their provenance identification. Previously, Maniatis *et al.*[22] and Mandi *et al.*,[18] conducted more in-depth and systematic research on the EPR spectrum of marble. Their findings were subjected to hierarchical aggregative cluster analysis, and 170 marbles constituted the first EPR database.[18] To date, this database has been extended significantly,[5,9,23] and a considerable number of archaeological marbles have been analyzed, with encouraging results.[2,4,14,24]

The underlying solid-state physics of this EPR-based information, is as follows: EPR identifies Mn^{2+} and Fe^{3+} in substitution of Ca^{2+} in the $CaCO_3$ of aged marble's surface.[9] Because the radius of Mn^{2+} (0.91 Å) is closer to that of Ca^{2+} (1.00 Å), it fits more easily into the calcite lattice without causing considerable disturbance. In contrast, Fe^{3+} (0.67 Å) generates far-greater crystallographic distortion and tends to access non-lattice locations in calcite rather than substitutional sites.[25] Re-crystallization results in the formation of freshly produced calcite crystals, which are anticipated to have lower impurity concentrations than marble crystals.[26] Water penetration induces re-crystallization but also enables Mn^{2+} and Fe^{3+} to enter marble surfaces in various oxidation states in clay minerals.[27] Additionally, the presence of fungi or bacteria promotes the entry of water and crystal dissolution, in addition to microbial oxidation or reduction of Fe and Mn on marbles' surfaces.[28]

Hereinafter, our working hypothesis was that all these geochemically or environmentally induced micro-alterations of the marble structures, could provide a correlating fingerprint of the marble's provenance. On this front, we focus on the study of local micro-alterations in marble crystals by combining EPR spectroscopy, ss-NMR spectroscopy, and XRD. In contrast to the classical use of XRD[17,29,30] *i.e.* as the standard method for crystal-phase identification in marbles, herein we elaborated on high-resolution analysis of the XRD focusing on the analysis of the microstrains of the crystallites.[31] Recently Yakaboylu *et al.*[31] have reported that strain analysis can provide distinct information on Marcellus Shales. Hereafter, our method relies on the assessment of structural microstrain by two methods (see conceptual Fig. 1 and 2): [i] X-ray diffraction line-broadening and [ii] zero-field-splitting (ZFS) tensor[32] from the EPR spectra of Mn^{2+} centers, naturally occurring in the marbles. The full details of the two methods and the definitions of the parameters are provided in Section 2.1, hereafter.

In brief, we define lattice-microstrain as an inhomogeneity of the lattice parameters, *i.e.*, the unit cell vector's alterations, with no change in the XRD diffraction angle position (Fig. 1), *i.e.*, no change in the average distance of the calcite or dolomite Miller planes $\{h\ k\ l\}$, see more explanation in Fig. 1. In this context, microstrain analysis through X-ray diffraction (XRD) provides information about the examination of the displacements of lattice-atoms from their ideal positions within a crystalline material. This provides valuable insights into the
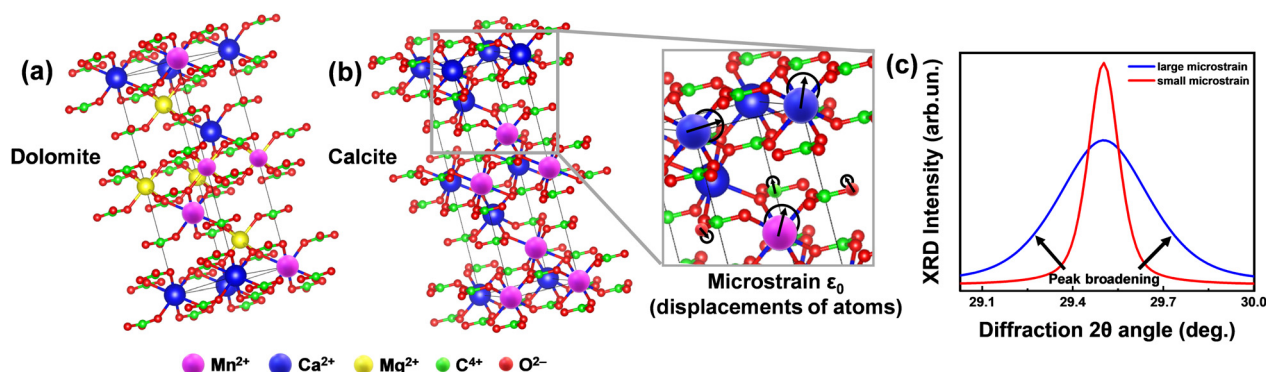
Fig. 1 Concept of microstrain analysis using XRD. (a) The unit cells of the predominant phases in Greek marbles, *i.e.* calcite (Ca(CO$_3$)) and dolomite (CaMg(CO$_3$)$_2$). (b) Magnified region of calcite's unit cell demonstrating the displacement of atoms. The degree of this relocation is captured by the microstructural (ε_0) analysis utilizing XRD and TOPAS software. (c) Theoretical XRD pattern of a crystallite under small (red line) and large (blue line) microstrain. We underline that since the size of the marble crystallite is in the micrometers range, see data in Table 4, the observed XRD-broadening in not due to nano-size effects, but exclusively due to lattice-strains.
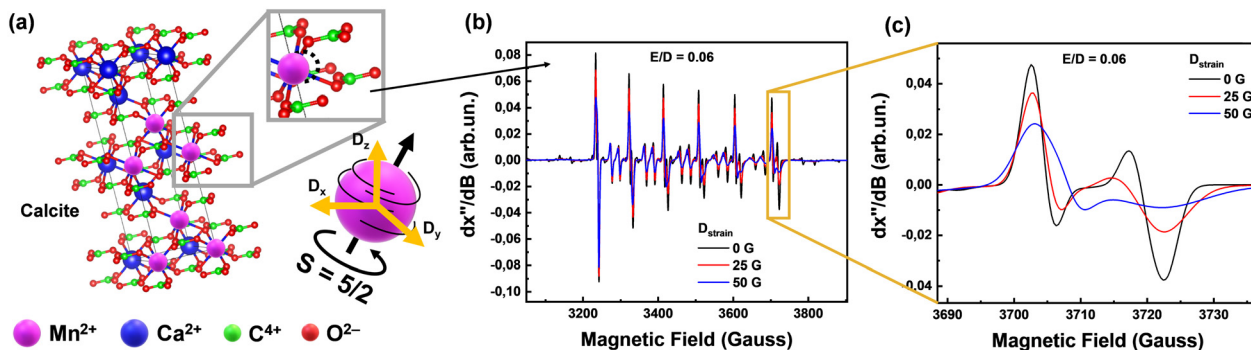
This journal is © the Owner Societies 2023

Phys. Chem. Chem. Phys., 2023, **25**, 31040–31049 | **31041**

Fig. 2 Phase composition of all collected Greek marbles contain calcite and dolomite. (a) Calcite unit cell of any marble, generated using VESTA software,[36] where we present a local displacement of Mn^{2+} in the lattice and therefore the strain which can be described as D_{strain} (orange arrows) *versus* the spin tensor (black arrows) direction. (b) EPR spectra which have different D distribution which displays changes of linewidths according to the D_{strain} value. (c) Magnified region of the last transition of the EPR Mn^{2+} sextet, demonstrating the D_{strain} linewidths changes.

level of lattice distortions within the marbles, aiding in the understanding of their mechanical properties, durability, and potential susceptibility to environmental factors.

The EPR signals from the $^{55}Mn^{2+}$ $(S = 5/2, I = 5/2)$ ions provide valuable information about their concentration and local environment, contributing to a deeper understanding of the composition and origin of the marbles.[22] Zero field splitting (ZFS) is a phenomenon that arises from the interaction between electron-spins in atoms with more than one-unpaired electron[33] *i.e.* $^{55}Mn^{2+}$ has five-unpaired electrons, thus $S = 5/2$. Moreover, the isotope ^{55}Mn has 100% natural abundance and is characterized by $I = 5/2$. Thus, the $S = 5/2$ and $I = 5/2$ of $^{55}Mn^{2+}$ provide a highly sensitive spin–probe system that sheds light on its immediate structural environment.[34] By analyzing the ZFS-tensor **D** (fully detailed in Section 2.1) of marbles, by EPR spectroscopy, we can gain insights into the atomic-level characteristics of the materials, such as the orientation of the magnetic-tensors and the distribution of the principal values of the **D**-tensor, that we define as D_{strain}, see more explanation in Fig. 2. Our key-hypothesis was that the ZFS-tensor D values and D_{strain} can act as sensitive probes to detect variations in the local microstructure among various homologous marble materials *i.e.*, reflecting their geochemical history and provenance.

In this context, herein we used electron paramagnetic resonance (EPR) spectroscopy *in-tandem* with X-ray diffraction (XRD) to study, on a systematic-comparative basis, a family of white marbles from various regions in Greece, see the map shown in Fig. 3. In addition, we have used high-temperature EPR[35] as an advanced, non-conventional, EPR technique to study the Mn^{2+}-ZFS in marbles *in situ* at elevated temperatures up to 700 K. This allowed us to investigate the possible role of temperature-induced strains in the materials and distinguish it from its interference with its geochemical EPR fingerprint.

Overall, the key aims of the present work were [i] to present a comprehensive correlation analysis of the structural, spectroscopic, and magnetic properties of various types of Greek marbles, including their crystal structure, lattice microstrain and $^{55}Mn^{2+}$ zero-field-splitting tensor strain and [ii] to propose the concurrent use of high-resolution-XRD and EPR as a novel
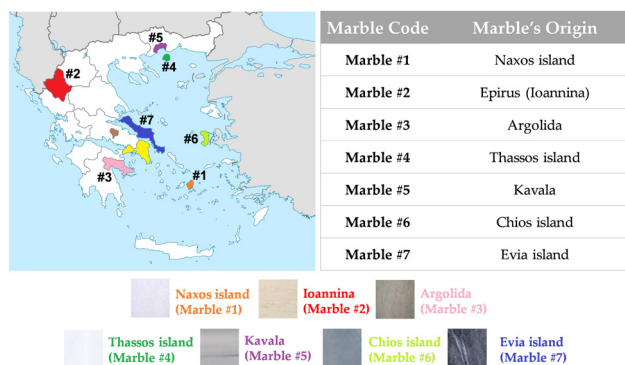

Fig. 3 Map with selected colored locations, from where marbles were collected. The Greek marbles were collected according to their color and historic importance.

methodological protocol to address questions of provenance, and thermal and geochemical history of marbles.

2. Experimental methods

2.1 Description of microstrain-analysis methods using XRD and EPR

The prevailing crystal phases for marbles are calcite $[Ca(CO_3)]$ and dolomite $[CaMg(CO_3)_2]$. Their unit cells are depicted in Fig. 2(a). The relocations of atoms from their ideal positions within the $Ca(CO_3)$ lattice (Fig. 2(b)) lead to XRD peak broadening, with no shift of the Bragg-diffraction angles. Microstrain represents displacements of atoms from their ideal positions, generated by any lattice imperfection (dislocations, vacancies interstitials and similar defects), eqn (1). It can be conceived by considering two extreme values of the lattice spacing d, namely $d + \Delta d$ and $d - \Delta d$, where $\varepsilon_0 = \Delta d/d$ is attributed as the mean deviation

$$\varepsilon_0 = \frac{\Delta d}{d} = \frac{\beta_{FWHM}(str)}{4 \tan\theta} \tag{1}$$

with $\beta_{FWHM}(str)$ representing the full-width-at-half-maximum of the XRD-peak related to microstrain broadening, and θ is the

31042 | *Phys. Chem. Chem. Phys.*, 2023, **25**, 31040–31049

This journal is © the Owner Societies 2023

diffraction angle. Thus, the larger the microstrain, the larger the XRD-peak broadening. (Fig. 1(c)). We underline that since the size of the crystallite is not altered *i.e.* typically in marbles it is in the *micro*meter range, see data in Table 4, the observed XRD-broadening in *not* due to nano-size effects, but exclusively due to lattice-strains.

Hereinafter, we have used high-resolution detection of the XRD signals, with angular steps of 0.01 degrees, and the use of TOPAS[37] software, to implement Rietveld analysis and micro-structure analysis. The concept of microstrain (ε_0) entails the deviations of atoms from their equilibrium positions within a crystal lattice, which are generated by different lattice imperfections such as dislocations, vacancies, interstitials, and similar defects.[38] By analyzing the broadening and shifting of diffraction peaks in the XRD pattern using TOPAS, the magnitude and distribution of microstrain in calcite and dolomite crystals can be quantitatively assessed.

The zero field splitting tensor (**D**-tensor) has three principal values (D_x, D_y, D_z) in its principal-axes system[32,33] see Fig. 2(a). The $D_{x,y,z}$ values are influenced by the electron–electron inter-actions within the $^{55}Mn^{2+}$ atom, which in turn are influenced by the immediate chemical environment of the atom.[23,33,34] Typi-cally, the $D_{x,y,z}$ values are influenced by factors such as ligand field strength, crystal symmetry, and local distortions.[32,34] These changes in D can be traced by EPR spectra *i.e.*, see examples of numerically simulated EPR spectra in Fig. 2(b) and (c). Importantly, as we exemplify in Fig. 2(b) and (c), D_{strain} can be reliably traced by EPR spectroscopy *via* alteration of certain spectral features *e.g.* the high-field transitions.

In this way, we have quantified and analyzed the lattice-microstrain (ε_0) by XRD and the ZFS, (D_{strain}), by EPR based on the definition and conventions defined herein.

2.2 Preparation of marble materials

The marble samples were collected as raw materials from different quarries in Greece, according to their historical loca-tions and their color, choosing from a colorful palette of Greek marbles that were used by many artists all over the centuries. In Fig. 3, we present a map of the regions where marbles were collected from. Marbles of different colors [marble #2 (Ioan-nina) yellowish, marble #6 (Chios Island) dark grey, marble #4 (Thassos Island) white] have different historic importance, *i.e.*, marble #1 from Naxos Island and marble #4 from Thassos Island are the two of great importance due to their large use in classical monuments and sculptures.

Firstly, the collected marbles were cleaned up by soft-tissue wiping, so that dirt and surface weathering were removed appropriately. Afterwards, the marbles were crushed to coarse powder of millimeter-size to avoid artefacts induced by the treatment. Comparison with intact pieces shows that coarse powders did not have additional treatment-induced signals. Therefore, the marbles used through all experiments for EPR, ssNMR and XRD analysis were in a coarse-powder form. In order to characterize the materials, we have collected sam-ples from three different spots from the same quarry site. The standard error is 5%.

2.3 Material characterization methods

Electron paramagnetic resonance. First, room temperature (300 K) or 77 K (liquid N_2) EPR spectra of marbles were recorded with a Bruker ER200D spectrometer, using a perpendicular-mode cavity model Bruker-ER4102ST. 15 mg samples were prepared and placed in 5 mm diameter quartz tubes, Suprasil Willmad. The experimental conditions were as follows: modulation amplitude = 10 Gpp; modulation frequency = 100 kHz; T = 300 K and 77 K for iron ions, see Fig. S1 (ESI†), microwave power = 20 mW; microwave fre-quency: 9.53 GHz.

High temperature EPR spectroscopy. High temperature EPR spectra were recorded with a Bruker ER200D spectrometer and a high temperature cavity model Bruker-ER41114HT. The pow-der samples were inserted into the high-T cavity using special zirconia-glass tubes obtained from Bruker. The experimental conditions were: modulation amplitude = 10 Gpp; modulation frequency = 100 kHz, microwave power = 5 mW, and microwave frequency = 9.57 GHz. The temperature was increased from T = 300 K up to 700 ± 0.1 K by a digitally controlled hot-N_2 gas flow, the heat control was achieved using a Bruker BVT3000, a BVTB3500 and monitored *in situ* in the ER41114HT cavity by a type-K thermocouple which is placed under the sample. At every temperature setting, the sample was allowed to equili-brate for at least 60 minutes and its spectral evolution was recorded. To verify the effect of long term thermal exposure, we have heated samples for up to 3 days in a lab-furnace. We found that within 30 minutes, the EPR spectrum attained a steady-state form at all temperatures. The g-values were calibrated using DPPH as the spin standard ($g = 2.0036 \pm 0.0003$).[39]

Theoretical simulation of $^{55}Mn^{2+}$ ($S = 5/2$, $I = 5/2$) EPR spectra. Numerical simulations of the EPR spectra were con-ducted using EasySpin, under MATLAB.[40] $^{55}Mn^{2+}$ spectral states with $S = 5/2$ and $I = 5/2$ were simulated using the spin Hamiltonian, eqn (2)[41]

$$\hat{H} = \beta\vec{B}\hat{g}\vec{S} + \vec{S}\ \mathbf{D}\vec{S} + \vec{I}\mathbf{A}\vec{S} \qquad (2)$$

where the first term is the Zeeman energy, the following two are the ZFS (zero-field splitting) interaction determined by D and E, the axial and rhombic zero field splitting tensor parameters respectively, and the last term is the hyperfine interaction of ^{55}Mn ($I = 5/2$).

Solid-state NMR (ssNMR). The collected marbles were pow-dered with an agate mortar to obtain 190 ± 5 mg to fill the 4 mm-diameter cross polarization magic angle spinning (CP-MAS) zirconium oxide rotor. The ^{13}C spectra were obtained on a 400 MHz Bruker Avance II spectrometer equipped with a CP-MAS probe. The spectra were recorded at the Department of Chemistry at the University of Ioannina. The rotation rate of the spin was at 8000 Hz for all the experiments, a single one-pulse sequence using a 90° nutation angle of 4 μs, a relaxation delay of 300 s and 256 scans. Two dummy scans were used to ensure a reproducible pre-saturation of the signal. For all the marbles, the measurement conditions (D1 at 300 s, number of scans at 256, dummy scans 2 and receptor gain at 512), the material

This journal is © the Owner Societies 2023

Phys. Chem. Chem. Phys., 2023, **25**, 31040–31049 | **31043**

mass was 190 ± 5 mg in all cases. Marble #1 was measured by incorporating with adamantane ($C_{10}H_{16}$) as a chemical shift standard for solid-state NMR. This signal was used to calibrate all NMR signals for all measured marbles.

X-Ray diffraction (XRD). The crystal structures of the materials were analyzed by XRD using a Bruker-D8 Advance diffractometer (Cu Kα radiation λ = 1. 5406 Å, 40 kV, 40 mA) at 2θ = $10°$–$130°$ (step size of $0.01°$ at a rate of 0.6 s per step). The average crystallite size was calculated using the Scherrer equation (eqn (3)):

$$d_{XRD} = \frac{K\lambda}{FWHM \cos\theta} \quad (3)$$

where d_{XRD} is the crystallite size (nm), k is a shape constant (in this case 0.9), λ is the wavelength of Cu Kα radiation (1.5406 Å), FWHM is the full width at half maximum and θ is the peak-diffraction angle.

3. Results and discussion

EPR and HT EPR spectroscopy

Fig. 4(a), presents a broad scan 77 K EPR spectra of all marbles. In all cases, the EPR spectrum characteristic of $^{55}Mn^{2+}$ (S = 5/2, I = 5/2) is detected.[34] A typical $^{55}Mn^{2+}$ EPR spectrum is characterized by six main peaks, corresponding to the allowed $2I + 1$ hyperfine splitting of –1/2 up to 1/2 transitions. Between each hyperfine, a pair of "forbidden" $\Delta M_I = 2$[34] peaks are present. In accordance with the original analyses conducted by Reed and Markham, their relative intensity and line shape, are governed by the numerical values of the components of tensors

D and A.[34] In marble structures, all these factors depend on the type of marble, its geological history, and the location of the marble.[4–6] The EPR spectra in Fig. 4 are due to Mn^{2+} ions occupying Ca-sites, in the unit cells of calcite or dolomite, see Fig. 2(a). The black lines in Fig. 4(a) are theoretically calculated $^{55}Mn^{2+}$ EPR spectra, using the spin Hamiltonian parameters listed in Table 1. Noticeably the hyperfine tensor anisotropy of all marbles did not vary significantly despite the different phase composition.

In Fig. 4(b), we show the EPR spectra of marbles #1, #4, and #7 that show significant differences. Such analysis, see the spin-Hamiltonian parameters in Table 1, provides two pieces of information as follows: [i] the hyperfine-tensor **A** values of the $^{55}Mn^{2+}$ (I = 5/2), and [ii] the **D**-tensor parameters together with its D_{strain} values. Accordingly, marble #7 shows two EPR spectral components corresponding to two types of Mn-atoms. Marble #7 is a pure calcite. Based on literature data,[42,43] the two Mn-atoms occupy two different calcium sites in the calcite structure, marked Ca-1 and Ca-2, in Fig. 4(b). As seen in Table 1 these two Mn^{2+} species are distinguishable by their different g-values, **D**-tensors and **A**-tensors. Site Ca-2 is characterized by smaller **D**-tensor values and lower D_{strain} i.e., 4 vs. 18 for the Ca-1 site. From the simulation of the EPR spectra, see Fig. 4(b), the relative population of these Mn^{2+}-centers is Ca-1 : Ca-2 = 0.7 : 0.3.

Their specific spin-Hamiltonian parameters are responsible for the clear differences seen in the EPR spectrum of marble #7, and, as we show in the following, can serve as fingerprints together with the XRD microstrain parameter (ε_0). Regarding marble #4, with a different phase composition, i.e. both calcite and dolomite, see XRD data in Table 4, we see that its ^{55}Mn-EPR spectrum can be deconvoluted into two sub-spectra, see Table 1. Based on literature data,[21–23] one ^{55}Mn-type (D-Mg-1 in Fig. 2(b) and (c)) refers to ^{55}Mn atoms occupying Mg-atom sites in dolomite, while D-Ca-1 in Fig. 2(b), corresponds to ^{55}Mn atoms occupying the Ca-atom sites in dolomite. From the EPR spectra, we estimate the relative populations of the two Mn^{2+} sites to be Mg : Ca = 0.96 : 0.04.

Both sites in marble #4 show moderate D_{strain} values of 10 and 15, respectively, see Table 1. Then, marble #1 which is pure calcite, shows a single EPR signal, see Table 1, from ^{55}Mn atoms occupying a Ca-atom site, see Ca-1 in Fig. 2(b). Marble #1 has a high D_{strain} of 21, see Table 1.

Based on the data listed in Table 1, hereafter we discuss four of them, according to their distinct phase compositions: marbles #2, #5, and #6 have a higher percentage of the calcite phase, in comparison with marble #4 with the dolomitic phase. The D_{strain} of these marbles spans a wide range of 10 up to 28, for Ca-sites and 15 for Mg-site in the dolomitic marble #4. We underline that the hyperfine tensor anisotropy of all marbles did not vary significantly, despite the different phase compositions.

In addition to the EPR analysis of pristine materials, the selected marbles #2, #4, #5, and #6 were studied using our high-temperature EPR spectrometer (see the EPR spectra in Fig. S2a–d of the ESI†). The protocol was as follows: for each material EPR
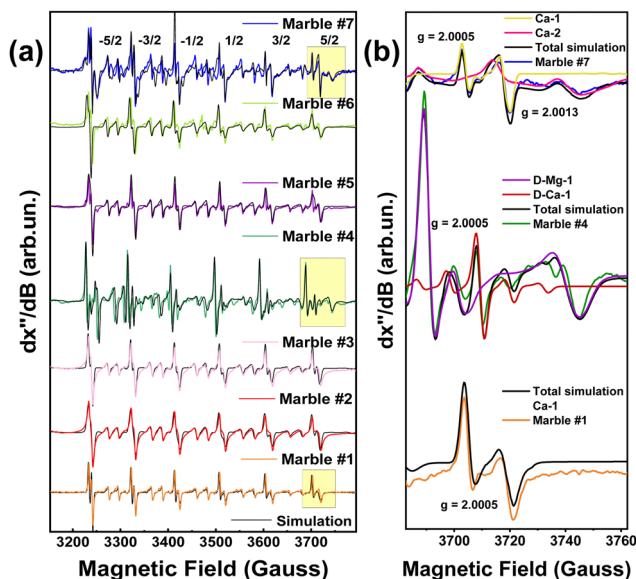

Fig. 4 (a) 77 K EPR spectra of all marble marbles. Due to traces of divalent manganese in substitution of some calcium or magnesium atoms in the lattice six double peaks are presented in the experimental. The EPR spectra were simulated via Hamiltonian quantification. Experimental conditions: modulation amplitude 10 Gpp, microwave power 32 mW, modulation frequency 100 KHz. (b) A selected range of EPR spectra was used to determine the different peaks and connect them with Ca and Mg-atoms.

31044 | *Phys. Chem. Chem. Phys.*, 2023, **25**, 31040–31049

This journal is © the Owner Societies 2023

Table 1 Spin Hamiltonian parameters of pristine Greek white marbles (#1–7)

Marble	g (±0.0001)			$[D, E]$ (Gauss) (±0.5)			D_{strain} (Gauss) (±1)			$[A_x, A_y, A_z]$ (Gauss) (±1)		
	Ca-site		Mg-site	Ca-site		Mg-site	Ca-site		Mg-site	Ca-site		Mg-site
#1	2.0004	—	—	[90, 5.4]	—	—	21	—	—	[94, 94, 93]	—	—
#2	2.0005	—	—	[86, 4.3]	—	—	23	—	—	[95, 94, 93]	—	—
#3	2.0005	—	—	[82, 5.3]	—	–	18	—	—	[95, 95, 93]	—	—
#4	2.0005	—	2.0005	[5.4, 0.1]	—	[160, 5.4]	10	—	15	[94.5, 95, 96]	—	[93, 93, 90]
#5	2.0005	—	—	[82, 4.6]	—	—	12	—	—	[93, 96, 93]	—	–
#6	2.0005	—	–	[90, 3.6]	—	—	28	—	—	[94, 96, 94]	—	—
#7	2.0005	2.0013	—	[107, 8.9]	[86, 5.4]	—	18	4	—	[88, 99, 95]	[95, 94, 93]	—

Table 2 Spin Hamiltonian parameters for the marbles (#2, 4, 5, and 6) at various temperatures (300–700 K)

Temperature (K) (±1)	A $[A_x, A_y, A_z]$ (Gauss) (±1)	$[D, E]$ (Gauss) (±0.5)	D_{strain} (Gauss) (±1)	g (±0.0001)
Marble #2				
300	[95, 94, 93]	[86.0, 4.3]	23	2.0005
400	[96, 94, 93]	[81.5, 4.4]	28	2.0005
500	[95, 94, 92]	[80.8, 4.6]	26	2.0005
600	[95, 94, 92]	[110.1, 4.5]	32	2.0005
700	[95, 94, 92]	[94.2, 4.3]	42	2.0005
Marble #4				
300	[94, 95, 95]	[5.4, 0.1]	10	2.0005
400	[95, 95, 95]	[5.6, 0.1]	14	2.0005
500	[95, 95, 95]	[5.8, 0.1]	16	2.0005
600	[95, 95, 95]	[5.3, 0.1]	17	2.0005
700	[95, 95, 95]	[5.5, 0.1]	20	2.0005
Marble #5				
300	[93, 96, 93]	[82.0, 4.6]	12	2.0005
400	[95, 95, 94]	[90.9, 4.6]	17	2.0005
500	[94, 95, 94]	[86.3, 4.6]	21	2.0005
600	[93, 95, 94]	[88.9, 4.6]	30	2.0005
700	[93, 95, 94]	[93.3, 4.6]	40	2.0005
Marble #6				
300	[94, 96, 94]	[90.0, 3.6]	28	2.0005
400	[94, 94, 93]	[87.8, 3.6]	29	2.0005
500	[94, 94, 93]	[88.3, 3.6]	30	2.0005
600	[94, 94, 93]	[96.2, 3.6]	38	2.0005
700	[94, 94, 93]	[92.8, 3.6]	47	2.0005

spectra were recorded *in situ* for temperatures up to 700 K, under an equilibration time of 2 hours for each temperature. After measurements the marbles were allowed to cool for 4 hours at room temperature ($T_{resting}$ = 300 K) and measured again (Fig. S3a–d, ESI†). In each case the EPR parameters measured at $T_{resting}$ were similar to those at high-T *i.e.* the changes in the value of D due to heat-stress were not reversible.

In Table 2, we present the Spin Hamiltonian parameters derived from the theoretical simulation of all experimental spectra for the four selected marbles at variable temperatures (300–700 K). For simplicity we discuss only the Ca-sites. The trends in D-parameters and the D_{strain} can be observed in Fig. 5(a) and (b) respectively, where we observe the following: [i] minor changes in the D-values for all marbles. Similarly, the rhombicity parameter E is not sensitive to the marble type, see Table 2. [ii] A significant increase of D_{strain} at increasing temperatures for all marbles. [iii] the D_{strain} increase was always more prominent in the calcite sites than in dolomite sites. Therefore, the present data exemplify that high-temperature electron paramagnetic resonance (EPR) provides a new tool to unravel microstrain trends in marbles. As shown in Fig. 5(a) an interesting fact is that with the increase in temperature all marbles show an increase in D_{strain} parameters, while D does not change. More specifically, marble #5 showed the most significant D_{strain} increase *i.e.*, 70% on heating from 300 to 700 K.

Marble #6 also showed a significant D_{strain} increase of 39% and marble #2 showed an increase of 45%. Marble #4 with a lower D_{strain} value showed an increase of 49%. Noticeably, a more careful perusal allows us to observe that the similarities between the D_{strain} trends for marbles #2, #5, #6 and their distinction *vs.* marble #4, might correlate with the [calcite/ dolomite] phase ratio, for example, the dolomitic (calcite/ dolomite = 3/96), marble #4 with low-initial D and D_{strain}, is
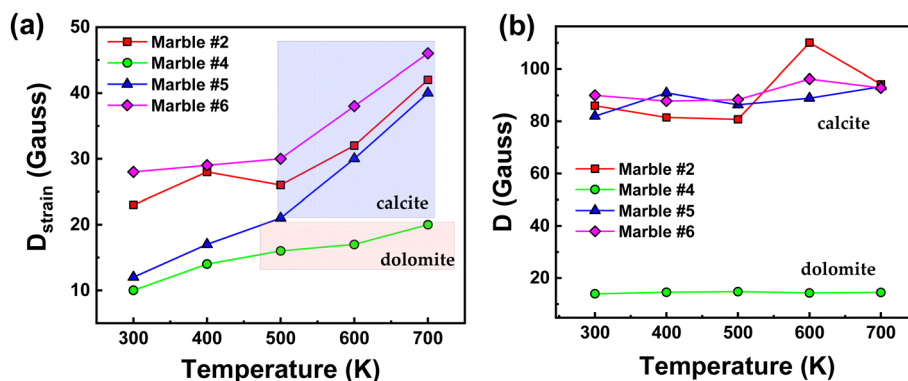
Fig. 5 Variations of (a) D_{strain} *vs.* temperature and (b) ZFS (**D**-tensor) *vs.* temperature, for marbles #2, #4, #5, and #6.
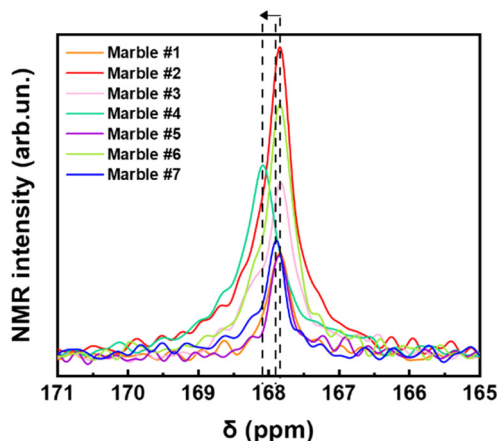
Fig. 6 ^{13}C NMR spectra of all marbles magnified in the carbonate's region.

more resistant to distortions at higher temperatures. On the other hand, marbles #2, #5, and #6 with mostly calcite phase composition show increased values of both D_{strain} and D, as well as D_{strain} sensitivity under thermal stress.[44]

To further peer into the microstructural features of these materials, marbles #2, #4, #5 and #6, we have studied their long-term exposure at 700 K for 30 minutes, 3 hours and 3 days. The XRD and EPR data are presented in Fig. S4 and S5 (ESI†), respectively, and the strain-trends *vs.* calcination time are listed in Tables S1 and S2 (ESI†). The plot of microstrain *vs.* the heating time (Fig. S6 and S7, ESI†) shows that in the first 3 hours an important strain increase occurs, while a minor change occurs upon further heating for up to 3 days. The high-T EPR data provide an additional piece of information, which further demonstrates that the D_{strain} (not D) is the parameter of

Table 3 ^{13}C solid state NMR spectral characteristic of Greek white marbles

Marble	δ (ppm)	$\Delta\nu_{1/2}$ (Hz)
#1	167.83	39.6
#2	167.83	47.5
#3	167.82	54.2
#4	168.07	60.7
#5	167.84	32.5
#6	167.83	46.9
#7	167.88	33.2

pertinence that is sensitive to the changes in the local environment.

^{13}C-Solid-state NMR

Fig. 6 shows a selected part of the ^{13}C-NMR spectra, (from 171 ppm to 165 ppm), the full spectra are shown in Fig. S8 (ESI†). In Fig. 6, we can decipher three parameters: the peak-position (δ in ppm), its width at half maximum ($\Delta\nu_{1/2}$), and the integrated area of resonance (Table S3, ESI†). The δ (ppm) and $\Delta\nu_{1/2}$ values are listed in Table 3. The calibrated δ-values show rather small variations of around 167–168 ppm that are assigned to ^{13}C of structural carbonates.[45] These structural carbonates in dolomite $[CaMg(CO_3)_2]$ or calcite $[Ca(CO_3)]$, are clearly distinct from free carbonates that are typically detected at 170.5 ppm.[20] The linewidths ($\Delta\nu_{1/2}$) listed in Table 3, vary in the range from 32.4 to 60.6 Hz depending on the marble. The carbonate peak broadening ($\Delta\nu_{1/2}$) may be caused either by the different distribution of the carbonates due to the presence of other atoms like Fe, Mn, and Mg, which can substitute Ca in the crystal lattice of calcite, or/and due to the presence of *para*/ferromagnetic substances/impurities.[46] From Table 3, we see that marble #4 has the highest percentage of dolomite with few ferro/paramagnetic impurities (see Table 4). This material shows higher $\Delta\nu_{1/2}$ = 60.6 Hz and ^{13}C δ shift. We see that these ^{13}C-strains are correlated with the highest structural micro-strains (ε_0), see XRD data in Table 5. Noticeably, the dolomitic marble #4 shows the lowest D and D_{strain} values of ^{55}Mn centers. All other marbles have almost the same δ-ppm and lack of dolomite phase. Marble #2 and #6, have Fe^{3+} ions and lastly marbles #1, #5 and #7 have the lowest concentration of ions in their structure.[47] Overall, the ^{13}C-NMR data provide additional information about the microstructure of the studied marbles. We underline that EPR, NMR and XRD probe different aspects of the marble structure, therefore, not a single method can provide material-discriminating information alone. As we show in the following, it is *the correlation* of the trends of the parameters that allows a better material-discriminating strategy to be built up.

Lattice-microstrain probed by X-ray diffraction

The XRD patterns for all marbles are presented in Fig. 7(a). As expected, they show that the predominant phases are calcite ($CaCO_3$) and dolomite ($CaMg(CO_3)_2$), with traces of quartz,
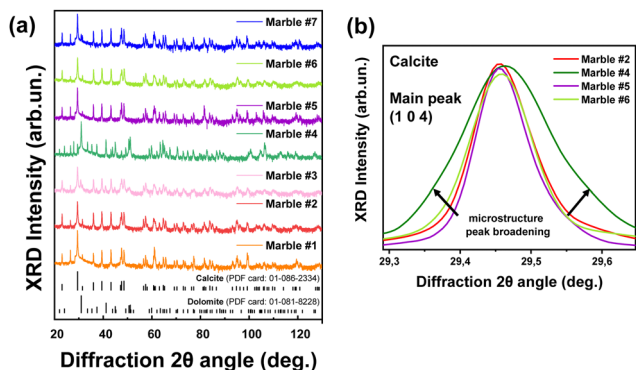
Table 4 XRD analysis, crystallite size and phase composition of the studied marbles

	Grain size d_{XRD} (μm)		Phase composition (%) (±0.5)					
	Calcite	Dolomite	Calcite	Dolomite	Magnetite	Quartz	Akermanite	Ankerite
Marble	$CaCO_3$	$CaMg(CO_3)_2$	$CaCO_3$	$CaMg(CO_3)_2$	Fe_3O_4	SiO_2	$Ca_2Mg(Si_2O_7)$	$Ca(Fe,Mg,Mn)(CO_3)_2$
#1	2.80 ± 0.27	—	95	—	—	5	–	—
#2	2.82 ± 0.12	—	96	—	1	1.5	1.5	—
#3	1.94 ± 0.12	2.63 ± 0.61	83	12	—	2	2	1
#4	2.81 ± 0.11	1.91 ± 0.16	3	96	—	1	—	—
#5	1.54 ± 0.14	—	96	—	—	4	—	—
#6	1.91 ± 0.12	—	95.5	—	—	2.5	1	1
#7	1.91 ± 0.16	–	94	—	1	2.5	2.5	—

31046 | *Phys. Chem. Chem. Phys.,* 2023, **25**, 31040–31049

This journal is © the Owner Societies 2023

Table 5 Microstrain (ε_0) of the marbles obtained by analysis of the XRD data

| Marble | Microstrain ε_0 ($\times 10^{-4}$) | |
| | Calcite | Dolomite |
	$CaCO_3$	$CaMg(CO_3)_2$
#1	4.1 ± 0.7	—
#2	4.7 ± 0.2	—
#3	7.1 ± 0.6	11.4 ± 1.1
#4	8.6 ± 0.4	9.6 ± 0.6
#5	2.9 ± 0.3	—
#6	4.0 ± 0.2	—
#7	3.2 ± 0.4	—

Fig. 7 (a) XRD patterns from collected Greek marbles and their major crystal phases, *i.e.* dolomite and calcite. (b) Magnified region of the main peak (1 0 4) of the Greek marbles, demonstrating the peak broadening as the microstrain increases.

magnetite, akermanite and ankerite (Table 4). All the observed diffraction peaks can be indexed to $CaCO_3$ with face-centered rhombohedral cell with trigonal symmetry ($\bar{3}m$), $a = 5.01$ Å, $b = 5.01$ Å, and $c = 16.99$ Å (JCPDS card no. 86-2340). The peaks at $23.06°$, $29.44°$, $31.43°$, $35.98°$, $39.42°$, and $43.16°$ are indexed

to the (012), (104), (006), (110), (113), and (202) Miller planes, respectively. Likewise, the dolomite peaks correspond to its trigonal phase with a rhombohedral lattice system, $a = 4.87$ Å, $b = 4.87$ Å, and $c = 16.19$ Å (JCPDS card no. 36-0426). The reflections centered at $24.04°$, $30.94°$, $33.54°$, $35.32°$, $37.38°$, and $41.13°$ with the corresponding (101), (012), (104), (006), (015), and (110) Miller planes belong to dolomite. The XRD data for all calcined materials are shown in Fig. S3 in the ESI.† In Table 4, the crystallite-size and phase composition are listed, as derived from analysis of the XRD data. The pure calcitic marbles are #1, #2, #5, #6 and #7, *i.e.* 'pure' means the majority of their composition is calcite, and in addition they possess traces of magnetite, quartz, akermanite and ankerite. Marble #3 is calcitic with a 12% dolomite, and marble #4 is pure dolomitic with a minimal $CaCO_3$ percentage of 3%.

Table 5 lists the derived microstrain values (ε_0) from the analysis of the XRD data. In all cases the microstrains are in the range $\varepsilon_0 = 3$–11×10^{-4}. In Fig. 8, we present correlation plots of the lattice-microstrain values (ε_0) derived from XRD *vs.* the D and D_{strain} values derived from EPR. We see that the microstrain ε_0 is larger for marbles #3 and #4 where dolomite or akermanite phases *i.e.*, Mg atoms are introduced in the crystal phase. When we examine the correlation trends (D *vs.* ε_0) and (D_{strain} *vs.* ε_0) in Fig. 8(a) and (b), we observe a diaspora of the points: marble #7 with its two ^{55}Mn D_{strain} values clearly identified at the left-hand part of Fig. 8(b). Marble #4 with its two species of $^{55}Mn^{2+}$, D and D_{strain} values is classified at the upper and lower parts of Fig. 8(a). Marble #1 with its two calcitic ε_0 values is shown in the middle parts of Fig. 8(a) and (b). More specifically, marble #4 where dolomite is 96% and calcite is 4%, has a low ZFS D-value of 12 Gauss while all marbles with more than 83% of calcite have a D range from 80 Gauss up to 110 Gauss. Microstrain analysis shows that all marbles with more calcite than dolomite phase composition, are in the range from 2.8×10^{-4} to 7.5×10^{-4}. Regarding the
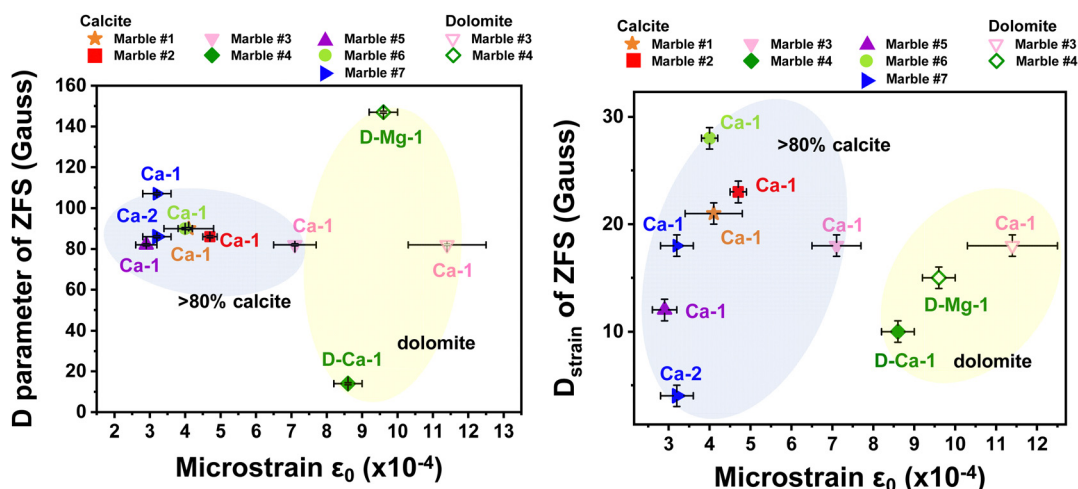
Fig. 8 Correlation plot ZFS-XRD microstrain. (a) D axial parameter *versus* XRD-microstrain ε_0 and (b) D_{strain} *versus* XRD-microstrain ε_0 for all the Greek marbles. We observe that when the marble is calcitic is positioned inside the blue bubble in the graph, while the dolomitic marbles are located in the yellow bubble. The points are notated as follows: Ca-1 for one species of calcite, Ca-2 for second species of calcite, D-Ca-1 for one species of calcite in dolomitic marble and D-Mg-1 for one species of dolomite in dolomitic marble (see Fig. 4(b)).

This journal is © the Owner Societies 2023

Phys. Chem. Chem. Phys., 2023, **25**, 31040–31049 | **31047**

D_{strain} *versus* microstrain ε_0, we observe similar correlation *i.e.*, for small microstrain values $\varepsilon_0 < 8.0 \times 10^{-4}$ we have calcitic marbles while for large $\varepsilon_0 > 8.0 \times 10^{-4}$ we have the interference of dolomite. The D_{strain} for pure calcitic marbles has a range of 0–30 Gauss, whilst the dolomitic marbles have a small range of 10–20 Gauss.

4. Conclusions

A novel methodology is suggested that correlates magnetic resonance properties with crystal-microstrain in order to reveal a trend that reflects the provenance of the marble. Greek marbles from different places along Greece, have been selected according to their historical importance and provenance and studied using our EPR, ssNMR and XRD methods. Theoretical simulation of the EPR spectra using the spin-Hamiltonian formalism, provides numerical values of the zero field splitting tensor (**D**-tensor) and its D_{strain} for each marble. High-temperature EPR provides, for the first time to our knowledge, important insight into the structural behavior of marbles under heat-stress that can be related to environmental events through history. Marbles with different phase compositions, *i.e.*, calcite and dolomite, show an increment of D_{strain} *versus* temperature. A pattern for marbles with more than 95% calcite is emerging which indicates a considerable D_{stain} for 12 Gauss up to 47 Gauss *versus* a temperature of 700 K. On the other hand, dolomitic marble #4 shows a lower range of **D**-tensor from 10 Gauss to 20 Gauss. XRD shows that calcitic marbles have low microstrain (ε_0), whilst the dolomitic ones have larger lattice-microstrain (ε_0) which indicates that the interference of Mg atoms (marbles #3 and #4) into the carbonate lattice affects the local crystal environment enhancing the lattice distortions. Finally, we propose a correlation plot between lattice-microstrain (ε_0) and the **D**-tensor strain from XRD data and EPR data, respectively. We consider that this correlation tool can be of broader use *i.e.*, to other marbles, as well as other cultural materials including ceramics and glasses with specific aims of deciphering the provenance and possibly historical path.

Conflicts of interest

There are no conflicts to declare.

Acknowledgements

Notes and references

1 *Ancient stones: quarrying, trade and provenance: interdisciplinary studies on stones and stone technology in Europe and Near East from the prehistoric to the early Christian period*, ed. M. Waelkens, N. Herz, L. Moens and Association for the Study of Marble and Other Stones used in Antiquity, Leuven University Press, Leuven, Belgium, 1992.

2 W. Prochaska, D. Attanasio and J. Archaeol., *Sci. Rep.*, 2021, **35**, 102676.

3 Y. Maniatis, D. Tambakopoulos, L. Lazzarini and M. C. Sturgeon, *Archaeometry*, 2021, **63**, 685–704.

4 D. Attanasio, M. Bruno, W. Prochaska and A. B. Yavuz, *Archaeometry*, 2015, **57**, 217–245.

5 K. Polikreti and Y. Maniatis, *Archaeometry*, 2002, **44**, 1–21.

6 V. Baïetto, G. Villeneuve, M. Schvoerer, F. Bechtel and N. Herz, *Archaeometry*, 1999, **41**, 253–265.

7 N. Herz and E. Garrison, *Treatise on Geochemistry*, Elsevier, 2014, pp.241–253.

8 D. Attanasio, R. Platania and P. Rocchi, *J. Archaeol. Sci.*, 2005, **32**, 311–319.

9 K. Polikreti and Y. Maniatis, *Atmos. Environ.*, 2004, **38**, 3617–3624.

10 I. Badouna, P. Koutsovitis, C. Karkalis, K. Laskaridis, N. Koukouzas, P. Tyrologou, M. Patronis, C. Papatrechas and P. Petrounias, *Minerals*, 2020, **10**, 507.

11 G. Charalampides, N. Arvanitidis, K. I. Vatalis and S. Platias, *Procedia Econ. Finance*, 2013, **5**, 143–151.

12 K. Al-Bashaireh, *J. Archaeol. Sci. Rep.*, 2021, **35**, 102777.

13 L. Moens, J. De Rudder, P. De Paepe and M. Waelkens, *Bull. Soc. Chim. Belg.*, 2010, **95**, 399–406.

14 G. Poretti, M. Brilli, C. De Vito, A. M. Conte, A. Borghi, D. Günther and A. Zanetti, *J. Cult. Herit.*, 2017, **28**, 16–26.

15 M. L. Gerdes, L. P. Baumgartner and J. W. Valley, *J. Petrol.*, 1999, **40**, 853–872.

16 P. Blanc, M. P. Lapuente Mercadal and A. Gutiérrez Garcia-Moreno, *Minerals*, 2020, **10**, 381.

17 J. D. Lynn, *All Days*, SPE, Al-Khobar, Saudi Arabia, 2011, p.SPE-149091-MS.

18 Y. Maniatis and V. Mandi, *J. Appl. Phys.*, 1992, **71**, 4859–4867.

19 A. Gutiérrez Garcia-M., M. C. Savin, N. Cantin, S. Boudoumi, P. Lapuente, R. Chapoulie and I. Pianet, *Archaeometry*, 2019, **61**, 795–808.

20 I. Pianet, A. Gutiérrez Garcia-Moreno, M.-C. Savin, N. Frerebeau, J. Trebosc, P. Florian and M. P. Lapuente Mercadal, *Materials*, 2023, **16**, 1468.

21 K. Polikreti, *Archaeometry*, 2007, **49**, 603–619.

22 Y. Maniatis, V. Mandi and A. Nikolaou, in *Classical Marble: Geochemistry, Technology, Trade*, ed. N. Herz and M. Waelkens, Springer, Netherlands, Dordrecht, 1988, pp. 443–452.

23 Y. Maniatis, Proc. Int. Sch. Phys. LdquoEnrico Fermirdquo, 2004, **154**, 179–202.

24 S. Khrissi, L. Bejjit, M. Haddad, C. Falguères, S. Ait Lyazidi and M. El Amraoui, *IOP Conf. Ser.: Mater. Sci. Eng.*, 2018, **353**, 012013.

31048 | *Phys. Chem. Chem. Phys.*, 2023, **25**, 31040–31049

This journal is © the Owner Societies 2023

25 J. D. Rimstidt, A. Balog and J. Webb, *Geochim. Cosmochim. Acta*, 1998, **62**, 1851–1863.

26 R. G. C. Bathurst, *Carbonate sediments and their diagenesis*, Elsevier, Amsterdam, 2nd edn, 1975.

27 D. Camuffo, M. Del Monte, C. Sabbioni and O. Vittori, *Atmos. Environ.*, 1982, **16**, 2253–2259.

28 D. A. Brown, D. C. Kamineni, J. A. Sawicki and T. J. Beveridge, *Appl. Environ. Microbiol.*, 1994, **60**, 3182–3191.

29 B. Bakruddin and A. R. Sembiring, *J. Inotera*, 2019, **4**, 79.

30 D. Covaci, C. Costea, D. Dumitras and O. G. Duliu, *Geophys. Res. Lett.*, 2012, **14**(EGU2012), 8771.

31 G. A. Yakaboylu, N. Gupta, E. M. Sabolsky and B. Mishra, *Int. J. Rock Mech. Min. Sci.*, 2020, **130**, 104345.

32 J. R. Pilbrow, *Appl. Magn. Reson.*, 1994, **6**, 161–181.

33 J. R. Pilbrow and G. R. Hanson, *Methods in Enzymology*, Academic Press, 1993, vol. 227, pp.330–353.

34 G. H. Reed and G. D. Markham, in *Biological Magnetic Resonance*, ed. L. J. Berliner and J. Reuben, Springer, US, Boston, MA, 1984, pp.73–142.

35 S. Zheng, J.-W. Feng and G. E. Maciel, *Energy Fuels*, 2005, **19**, 1201–1210.

36 K. Momma and F. Izumi, *J. Appl. Crystallogr.*, 2008, **41**, 653–658.

37 R. E. Dinnebier, A. Leineweber and J. S. O. Evans, *Rietveld Refinement: Practical Powder Diffraction Pattern Analysis using TOPAS*, Berlin, Boston: De Gruyter, 2019, DOI: **10.1515/9783110461381**.

38 Y. Zhao and J. Zhang, *J. Appl. Crystallogr.*, 2008, **41**, 1095–1108.

39 D. Sanna, G. Delogu, M. Mulas, M. Schirra and A. Fadda, *Food Anal. Methods*, 2012, **5**, 759–766.

40 S. Stoll and A. Schweiger, *J. Magn. Reson.*, 2006, **178**, 42–55.

41 C. R. Byfleet, D. P. Chong, J. A. Hebden and C. A. McDowell, *J. Magn. Reson.*, 1969, **1970**(2), 69–78.

42 C. R. De Abreu, T. C. Cordeiro, A. A. G. Carrasquilla, E. S. De Souza and A. O. Guimarães, *J. Pet. Sci. Eng.*, 2021, **203**, 108847.

43 R. A. Shepherd and W. R. M. Graham, *J. Chem. Phys.*, 1984, **81**, 6080–6084.

44 C. Ionescu, V. Hoeck, C. Gruian and V. Simon, *Appl. Clay Sci.*, 2014, **97–98**, 138–145.

45 K. Beshah, C. Rey, M. J. Glimcher, M. Schimizu and R. G. Griffin, *J. Solid State Chem.*, 1990, **84**, 71–81.

46 V. J. Witherspoon, J. Xu and J. A. Reimer, *Chem. Rev.*, 2018, **118**, 10033–10048.

47 H. Nebel, M. Neumann, C. Mayer and M. Epple, *Inorg. Chem.*, 2008, **47**, 7874–7879.

This journal is © the Owner Societies 2023

Phys. Chem. Chem. Phys., 2023, **25**, 31040–31049 | **31049**